

Fast calculation of capacitances in silicon sensors with 3D and 2D numerical solutions of the Laplace's equation and comparison with experimental data and TCAD simulations

P. Assiouras,^{a,1} P. Asenov,^a A. Kyriakis^a and D. Loukas^a

^a*Institute of Nuclear and Particle Physics (INPP), NCSR Demokritos
Agia Paraskevi, Greece*

E-mail: panagiotis.assiouras@cern.ch

ABSTRACT: We have developed a software for fast calculation of capacitances in planar silicon pixel and strip sensors, based on 3D and 2D numerical solutions of the Laplace's equation. The validity of the 2D calculations was checked with capacitances measurements on Multi-Geometry Silicon Strip Detectors (MSSD). The 3D calculations were tested by comparison with pixel sensors capacitance measurements from literature. In both cases the Laplace equation results were compared with simulations obtained from the TCAD Sentaurus suite. The developed software is a useful tool for fast estimation of interstrip, interpixel and backplane capacitances, saving computation time as a first approximation before using a more sophisticated platform for more accurate results if needed.

KEYWORDS: Particle tracking detectors (Solid-state detectors); Simulation methods and programs; Si microstrip and pad detectors; Detector modelling and simulations II (electric fields, charge transport, multiplication and induction, pulseformation, electron emission, etc)

¹Corresponding author.

Contents

1	Introduction	1
2	Numerical solution of the Laplace's equation	2
2.1	Three dimensional solution	2
2.2	Two dimensional solution	4
3	TCAD Simulations	4
3.1	Strip sensors	5
3.2	Pixel sensors	6
4	Experimental measurements and comparison with simulation	7
4.1	Geometry of strip sensors and experimental setup	7
4.1.1	Strip backplane capacitances	8
4.1.2	Interstrip capacitances	9
4.2	Comparison of 3D Laplace solver with experimental data of various pixel geometries	11
4.3	Comparison between TCAD and 3D Laplace solver for various pixel geometries	14
4.4	Comparison of the runtime between the two simulations	16
5	Conclusion	16
A	Properties used for the TCAD simulations	17

1 Introduction

Silicon sensors are extensively used in High Energy Physics experiments as tracking detectors of charged particles. The most commonly used planar silicon detectors in High Energy Physics experiments are devices segmented into strips (micro-strip detectors) or pixels (micro-pixel detectors). Important parameters in the operation and the design of silicon detectors are the capacitances between adjacent strips or pixels and between the strips or pixels and the backplane. These capacitances are related to signal to noise ratio as well as crosstalk phenomena between neighboring pixels or strips.

A numerical algorithm for solving the three dimensional Laplace's equation and calculating the capacitances of a pixel sensor, was presented in [1]. A reduced form of the algorithm has been implemented for calculating the capacitances of micro-strip sensors by solving the Laplace's equation in two dimensions. Through these algorithms, numerical calculations of the capacitances between adjacent strips or pixels as well as the capacitances between the strips or pixels and the backplane can be made. These algorithms have been implemented within a software that can be used as a simulation tool for a fast estimation to lower order of the above mentioned capacitances.

Calculations for the pixel sensors obtained with our method are compared with published experimental data and TCAD simulations on various configurations of pixel geometries. Calculations for strip sensors, are compared with experimental results and TCAD simulations on multi-geometry strip sensors (MSSD). The MSSD sensors were kindly provided by the Outer Tracker Sensor working group for the Phase-2 upgrade of the CMS/LHC collaboration [2].

2 Numerical solution of the Laplace's equation

In the current section we give an outline of the method, for a detailed presentation see [1]. A key characteristic of this method is that the axes that are parallel to the pixel or strip plane are discretized in finite elements, while the perpendicular axis is kept continuous. Then by using a Fourier transform, the three dimensional problem for the pixel sensors is reduced to two dimensions and the two dimensional problem for the strip sensors is reduced to one dimension. The problem is then solved in Fourier space by using a numerical method.

2.1 Three dimensional solution

Figure 1 shows the capacitive network of a pixel detector. The capacitances that are calculated with this method are those formed between the central pixel and the adjacent pixels in the directions that are parallel to x - and y - axis respectively (C_{01} and C_{02}), the capacitances that are formed between the central pixel and the adjacent pixels in the diagonal direction (C_{03}) and the capacitances that are formed between each pixel and the backplane (C_{00}). These capacitances are strongly related to the geometry features of the sensor such as the dimensions of each pixel and the separation gap between them and the thickness.

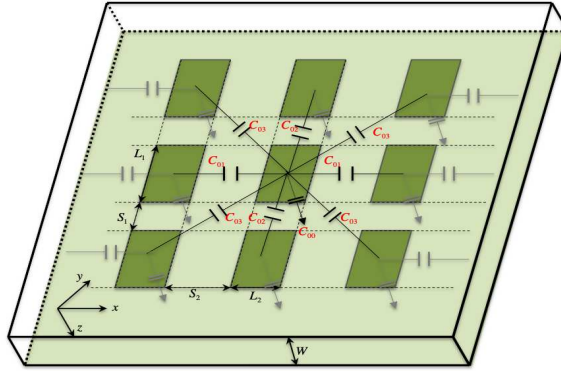


Figure 1: Schematic of the capacitive network of a pixel sensor with 9 pixels. C_{01} and C_{02} are the capacitances that are formed between the central and the adjacent pixels in the directions that are parallel to the x - and y - axis respectively. C_{03} are the capacitances that are formed between the central and the adjacent pixels in the diagonal direction and C_{00} are the capacitances that are formed between each pixel and the backplane.

To calculate the strip sensor capacitances the Poisson's equation is solved with normalized boundary conditions by setting $V(x, y, z) = 1$ at the central pixel and $V(x, y, z) = 0$ at the adjacent pixels and the backplane. In the areas not covered by pixel the equation $(\epsilon_{Si} E_{Si}(x, y, z) -$

$\varepsilon_a E_a(x, y, z) = 0$) is applied for keeping the electric field in the interface continuous, where ε_{Si} , ε_a are the dielectric constants and $E_{Si}(x, y, z)$, $E_a(x, y, z)$ are the vertical components of the electric field in silicon and ambient space, respectively. The ambient space in this work is considered to be air.

The detector is considered to be in a fully depleted state and it is free from thermally generated free charge carriers (pairs of electrons and holes). This is the state in which a realistic silicon detector works, when a reverse bias voltage is applied to the silicon sensor and the depleted region is formed. The thermally generated free charged pairs of electrons and holes are swept from the electric field creating an ionization chamber. The pixels are assumed to be infinitesimally small in depth compared to the fully depleted region of the detector. Also, for simplicity it is considered that the volume and the surface of the detector are free from static charges. Under real circumstances, charges exist inside the detector volume. These are stripped ions in the depleted regions and defects from contamination inside the material. However, they produce an electric field component which is independent of the biasing voltage. The charges add a voltage-independent term in the expression of the strip charge which does not influence the calculation of the capacitance.

Under the aforementioned assumptions Poisson's equation is reduced to the Laplace's equation 2.1. Subsequently, by using Fourier transform, while keeping the perpendicular axis continuous, the three dimensional problem is reduced to two dimensions (equation 2.2). For details see ref. [1].

$$\nabla^2 V(x, y, z) = 0 \xrightarrow{\mathcal{F}} \quad (2.1)$$

$$\frac{\partial^2 V(k_x, k_y, z)}{\partial z^2} = (k_x^2 + k_y^2) V(k_x, k_y, z) \quad (2.2)$$

where $V(k_x, k_y, z)$ is the potential in Fourier space and k_x, k_y the corresponding coordinates in Fourier space. By solving the differential equation with the appropriate boundary conditions, equation 2.3 is derived which gives the electric field in Fourier space ($E_z(k_x, k_y, 0)$) as a function of the potential in Fourier space ($V(k_x, k_y, 0)$), which for $z = 0$ corresponds to the pixel plane, where w corresponds to the detector thickness and $F(k_x, k_y)$ is a function of the Fourier coefficients.

$$E_z(k_x, k_y, 0) = F(k_x, k_y) \frac{1 + e^{-2F(k_x, k_y)w}}{1 - e^{-2F(k_x, k_y)w}} V(k_x, k_y, 0) \quad (2.3)$$

The Laplace's equation is then solved in the Fourier space by using a self-consistent numerical method. First an initial guess of the potential is made $V_{init}(x, y, 0)$ where for ($z = 0$) it corresponds to the pixel plane. By using Fourier transform, with respect to x - and y - axis the initial guess is transformed to the potential in Fourier space $V_{init}(k_x, k_y, 0)$. Then the vertical component of the electric field inside the sensor $E_{Si}^{init}(x, y, 0)$ is calculated from 2.3 by performing inverse Fourier transform. The vertical component of the electric field in the ambient space $E_a^{init}(x, y, 0)$ is calculated by equation 2.3 setting ($w \rightarrow \infty$) and using inverse Fourier transform. Next the potential is redefined by boundary conditions. The values of the vertical component of the electric field in the ambient space $E_a^{init}(x, y, 0)$ are used for calculating the new values of the electric field inside the sensor $E_{Si}^{init}(x, y, 0)$, by using the boundary condition in the space that is not covered by pixels. This gives a new estimation of the electric field inside the sensor $E_{new}(x, y, 0)$ and a new

estimation of the potential $V_{new}(x, y, 0)$. The actual solution of the problem is assumed to be a linear combination of the new and the initial potential functions. Then a check for convergence is made and if it has not been achieved the initial function is set equal to the new potential functions, that has been derived from the linear combination. All the above steps are repeated through several cycles until convergence is reached.

Finally, once convergence has been achieved, the charges stored in each pixel are calculated by integrating the charge density in the whole pixel surface ($Q = \iint (\epsilon_{Si} E_{Si} - \epsilon_a E_a) dS$). Then the calculation of pixel capacitances is made.

2.2 Two dimensional solution

This algorithm can be used for calculating the capacitances in micro-strip detectors with planar geometry. Figure 2 shows the capacitive network of a strip sensor with 7 strips.

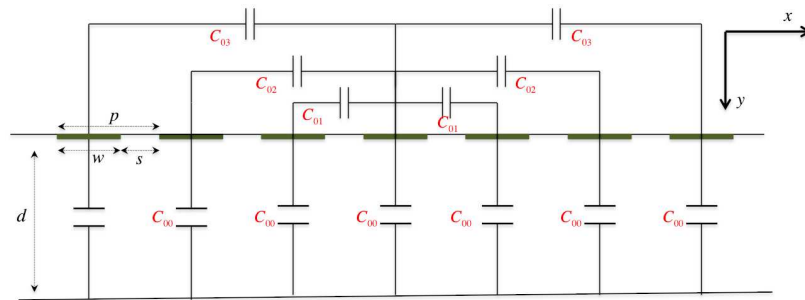


Figure 2: Schematic of the capacitive network of a micro-strip detector with 7 strips. C_{01} are the capacitances between the central and the first adjacent strip, C_{02} between the central and the second adjacent strip, C_{03} between the central strip and the third adjacent strip, and C_{00} between each strip and the backplane, where w is the strip width, s is the interstrip space and p is the strip pitch and d is the detector thickness

The capacitances that are calculated with this algorithm are those between a central strip and the backplane (C_{00}), the capacitances between the central and the first adjacent strips (C_{01}) and between the central and the second adjacent strips (C_{02}). While the software calculates capacitances up to the third (C_{03}), these are negligible and omitted from our study. The same method as in the three dimensional case is followed, with the difference that in the strip sensor case the problem is reduced to two dimensions and by using Fourier transform the Laplace's equation is solved in one dimension. In this case the axis that is parallel to the strip plane (x - axis) is discretized in finite elements, while the perpendicular (y - axis) is kept continuous.

3 TCAD Simulations

Technology computer-aided design (TCAD) is used in the semiconductor industry in order to develop and optimize semiconductor processing technologies and devices. It can be used in order to simulate the fabrication procedure, the operation and the reliability of the semiconductor devices. The TCAD suite that was used for this work is the commercial software package TCAD Sentaurus from Synopsys [3].

TCAD follows a finite element analysis scheme. Firstly, the device is designed in two or three dimensions and the properties of each region of the device, such as the doping concentration, the materials or shape are defined. Another way to create a device is by simulating the actual fabrication procedure, but this approach is beyond the scope of the present work. Afterwards the device is subdivided into finite elements by following a Delaunay triangulation algorithm [4] which creates a mesh of the device.

The next step is to activate the desired physical models and parameters before initiating the device simulation program. Some of the physical models that were used in this work are the Auger recombination, Shockley-Read-Hall recombination, avalanche electron-hole generation, trap-to-trap recombination, band-to-band tunneling, doping dependence mobility, high field saturation and carrier-carrier scattering [5].

The fundamental partial differential equations for semiconductors (Poisson's, continuity equations for electrons and holes) are solved at each of the generated mesh point and the desired physical quantities are calculated. In order to calculate the capacitances a small signal AC analysis is performed at 1 kHz for the backplane capacitance and at 1 MHz for the interstrip capacitance. These frequencies correspond to the frequencies that the experimental measurements of this sensors were performed.

3.1 Strip sensors

Figure 3 shows the simulated structure of the MSSDs. The design resembles a perpendicular cross-section of the sensor to the strip plane. The final results are scaled to the actual sensor strip length. The structure has 5 strips instead of 32 of the actual MSSD sensors with implant and aluminum widths as denoted in table 1. The different layers of each strips are depicted in the top-right part of figure 3 as well as the generated mesh consisting of triangular segments. The metal depicted in gray is extended a few μm in the interstrip space. This technique is called metal-overhang and is used in order to overcome the junction curvature effect which limits the breakdown voltage of planar junctions [6], [7]. In the space between two strips two additional structures (depicted in cyan) have been designed with high dose of p-implant resembling the actual p-stop structures of the sensor. The bulk doping concentration is assumed to be equal to $3.5 \times 10^{12} \text{ cm}^{-3}$ (p-type), while the strip doping concentration is assumed to be equal to $1.0 \times 10^{19} \text{ cm}^{-3}$ (n-type). The deep diffusion technique on the backplane is simulated by using an error function doping profile. More details on the parameters that were used in order to produce these simulations can be seen in Appendix A. Most of the parameters that are used in the simulation have been chosen by following the works presented in [8] and [9].

The interstrip capacitance between two strips i and j for an AC coupled sensor are calculated, according to [10], with the following formula 3.1.

$$C_{int} = C_{M_i-M_j} + C_{I_i-I_j} + C_{M_i-I_j} + C_{I_i-M_j} \quad (3.1)$$

where $C_{M_i-M_j}$ is the capacitance between the metal of the i^{th} strip and the metal of the j^{th} strip, $C_{I_i-I_j}$ is the capacitance between the implant of i^{th} strip and the implant of j^{th} strip, $C_{M_i-I_j}$ is the capacitance between the metal of i^{th} strip and the implant of j^{th} strip, $C_{I_i-M_j}$ is the capacitance between the implant of i^{th} strip and the metal of j^{th} strip.

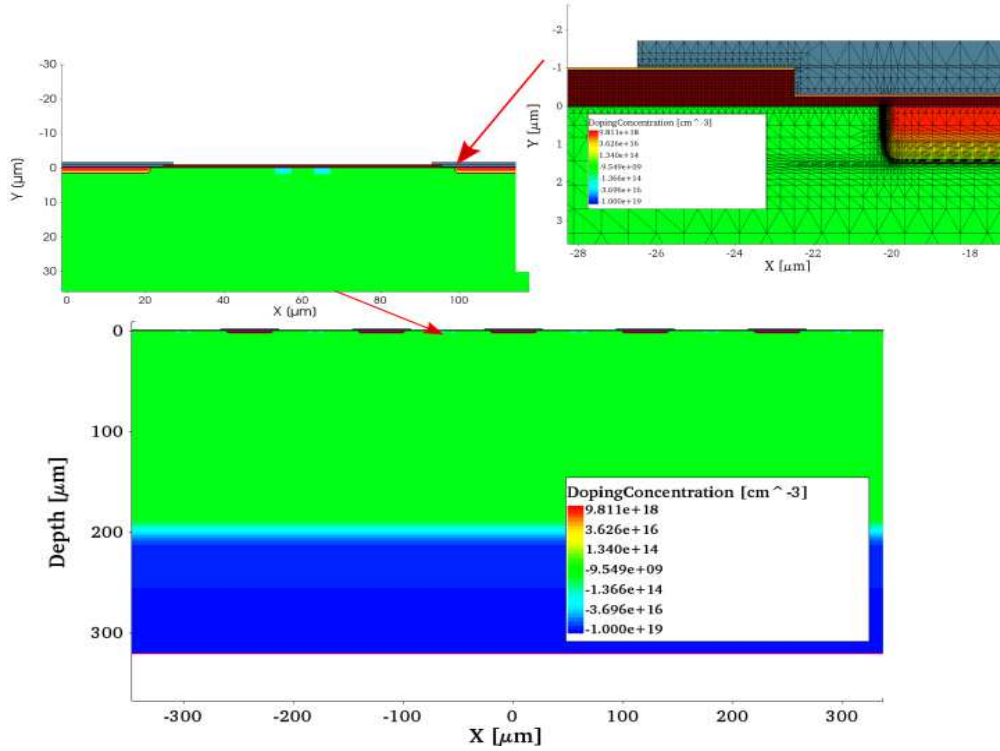


Figure 3: The structure that was used for simulating the MSSD sensors. In the bottom middle the whole structure that was used with 5 strips is shown. The color variation depicts the doping concentration. The top-left figure shows a close up view between two strips. Two p-stop structures are designed, depicted in cyan, in order to achieve strip isolation. The top-right figure shows a close-up view of the simulated structure near to one strip edge. The n-type implant is displayed in red which is simulated with a Gaussian profile, the aluminum contacts are displayed with gray, the SiO_2 is displayed with brown and the p-type silicon bulk is displayed with green.

3.2 Pixel sensors

For pixel sensors a 3D simulation approach is employed. The simulated structures consist of 9 orthogonal pixels with two different pixel geometries one with pixel area of $50 \times 50 \mu m^2$, (figure 4a), and one with pixel area of $100 \times 25 \mu m^2$, (figure 4b). Both structures are DC-coupled with a n^+p configuration and an active thickness of $150 \mu m$. A guard ring structure surrounds the device, providing a homogeneous electric field inside the sensitive area and minimizing the edge effects. The simulations were made for different pixel layouts with varying separation gap between $5 \mu m$ to $50 \mu m$ with a $5 \mu m$ step. The capacitances were calculated by performing a small signal AC analysis with frequencies at 1 kHz and 1 MHz for the backplane and interpixel capacitances, respectively. These are the configurations under development for the Phase-2 upgrade of the CMS/LHC [2] and Atlas/LHC [11] silicon trackers at CERN. Simulation parameters are shown in Appendix A.

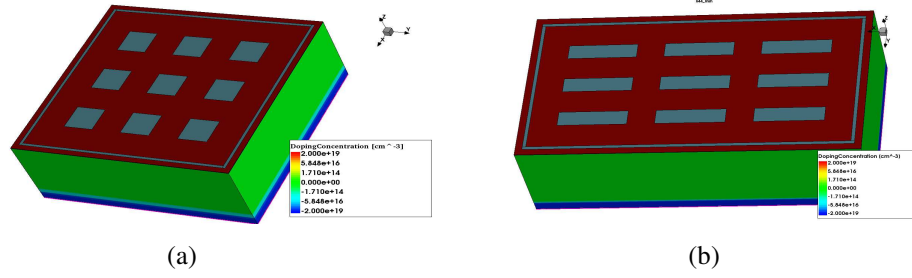


Figure 4: Simulated structure for pixel sensors with $50 \times 50 \mu\text{m}^2$, (figure 4a) and with $100 \times 25 \mu\text{m}^2$, (figure 4b) pixel area.

4 Experimental measurements and comparison with simulation

4.1 Geometry of strip sensors and experimental setup

Figure 5 shows an actual picture of a Multi Geometry Silicon Strip Detector (MSSD). The MSSDs contain 12 individual regions and they all have their own bias and guard rings. Each region contains 32 AC coupled strips on n⁺p configuration with pitches varying from 70 to 240 μm resulting to width-to-pitch ratios (w/p) varying from 0.133 to 0.321. The geometrical characteristics of each region are described in table 1. More details for these sensors can be found in [12]. The multi-geometry of these sensors allows the study of capacitances with different width to pitch ratios to be made. This makes them a suitable choice for checking the calculation capability of our software for various strip geometries.

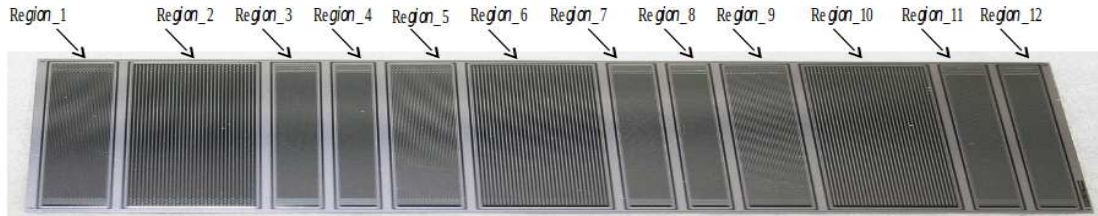


Figure 5: A Multi-Geometry Silicon Strip Sensor. The sensor has 12 regions with different pitches and width-to-pitch ratio (w/p). Three of these sensors with physical thickness of 320 μm and active thickness of 120, 200 and 320 μm used for the measurements

Table 1: Geometrical characteristics of the MSSD sensors for each region.

Label	1(120)	1(240)	1(80)	1(70)	2(120)	2(240)	2(80)	2(70)	3(120)	3(240)	3(80)	3(70)
Region	1	2	3	4	5	6	7	8	9	10	11	12
Pitch	120	240	80	70	120	240	80	70	120	240	80	70
Width	16	34	10	8.5	28	58	18	15.5	40	82	26	22.5
Width of Al	29	47	23	21.5	41	71	31	28.5	53	95	39	33.5
w/p	0.133 (0.142)	0.142 (0.146)	0.125 (0.138)	0.121 (0.136)	0.233 (0.242)	0.242 (0.246)	0.225 (0.238)	0.221 (0.236)	0.333 (0.342)	0.342 (0.346)	0.325 (0.338)	0.321 (0.336)

The three MSSD sensors that we measured in this work originate from 3 different wafers of float zone silicon (FZ). They have the same physical thickness of 320 μm , but three different active thicknesses of 120 μm (FZ120P), 200 μm (FZ200P), 320 μm (FZ320P). The manufacturer achieves this by a deep diffusion technique. In order to achieve isolation of the strip implants an additional high dose of p+ implantation is made between the strips surrounding each n+ strip. These structures are called p-stop.

The measurements were performed with a semi-automated probe station (Carl Susse PA 150). The whole setup was electrically shielded inside a light-tight metal box. The capacitances are measured with an HP4192A LCR meter which supplies a small AC signal superimposed upon the DC bias voltage on the HIGH terminal. The amplitude and phase are measured on the LOW terminal. Backplane capacitances were measured by using the bias ring which connects together all the 32 strips via the bias resistors. The measurements were performed at a frequency of 1 kHz with an amplitude of 250 mV. The bias voltage (detector HI) was applied to the backplane while the bias ring was grounded. The bias voltage was ramped up from 0 V to 400 V. The interstrip capacitances were measured by performing an automatic strip scan in each strip, of each region, of the sensor. In this measurement, two neighboring strips were contacted with the probes connected one with the HI terminal along with the backplane and the strip under test to the LOW terminal. The interstrip capacitance measurements were performed at 1 MHz with an amplitude of 250 mV. The frequencies and the amplitudes that have been chosen correspond to those that yield the optimum C-V characteristics of these sensors with the particular experimental setup for the backplane and interstrip capacitances respectively.

4.1.1 Strip backplane capacitances

Histograms 6a, 6b and 6c show the comparison between the backplane capacitances for the 3 MSSD sensors. The regions 3 and 12 in the FZ200P sensor and 2 and 9 in the FZ320P sensor were damaged. In the majority of the measured samples with different w/p ratio the measured backplane capacitance is larger than the simulated one, probably due to parallel parasitic capacitances introduced during the measurement. The TCAD simulated capacitance seems to be closer to the measured one in the majority of our samples. However, our simpler but much faster Laplace solver gives quite comparable results for the backplane capacitance.

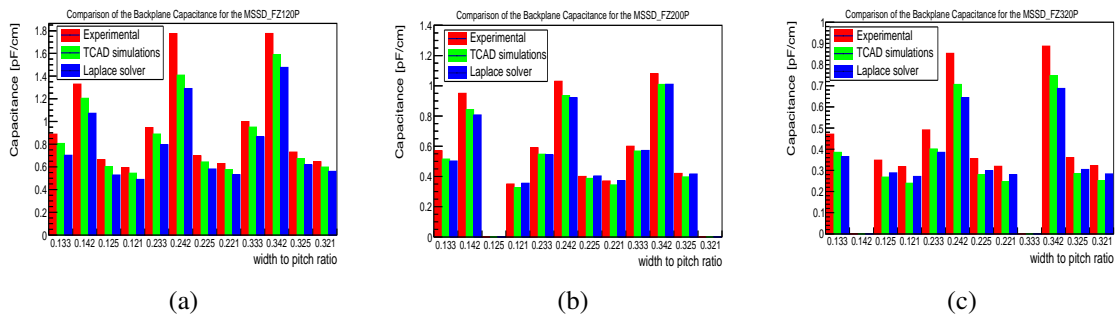


Figure 6: Comparison of the experimental results (red), the results of the related TCAD simulations (green) and the Laplace solver (blue) for the backplane capacitance in FZ120P 6a, FZ200P 6b and FZ320P 6c sensors.

Figures 7a and 7b show the relative errors of the backplane capacitance defined as $(C_{exp} - C_{sim})/C_{exp} \%$, of the backplane capacitance where C_{sim} are the simulated results from our Laplace solver and the TCAD simulations respectively and C_{exp} are the experimental values. A Gaussian fit is also shown for comparison. The numerical calculations made with the Laplace solver have a mean value of 14% with a standard deviation of 7% while the calculations made with TCAD have a mean value of 12% and a standard deviation of 6%.

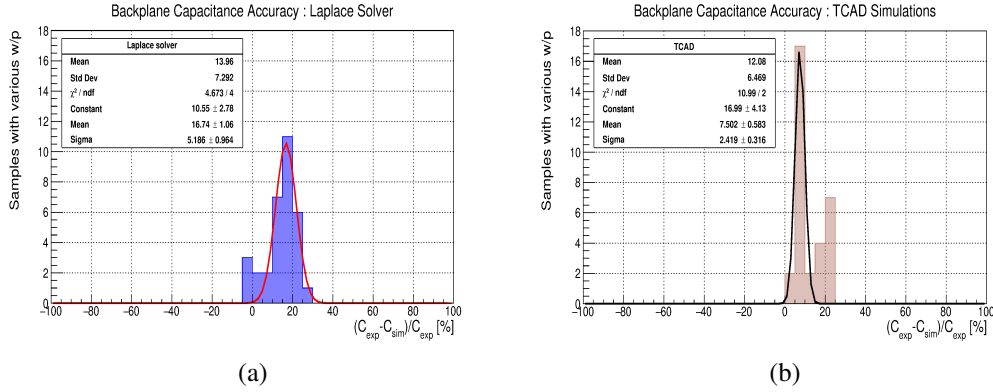


Figure 7: Histograms of the relative error of the simulated results to the experimental values for the backplane capacitance for the Laplace solver 7a and for the TCAD simulations 7b from all 3 MSSD sensors

4.1.2 Interstrip capacitances

Histograms 8a , 8b and 8c show measured and simulated interstrip capacitances for the 3 MSSD sensors. As in the backplane case, in the majority of the measured samples with different w/p ratio the measured interstrip capacitance is larger than the simulated one, probably due to parallel parasitic capacitances introduced during the measurement.

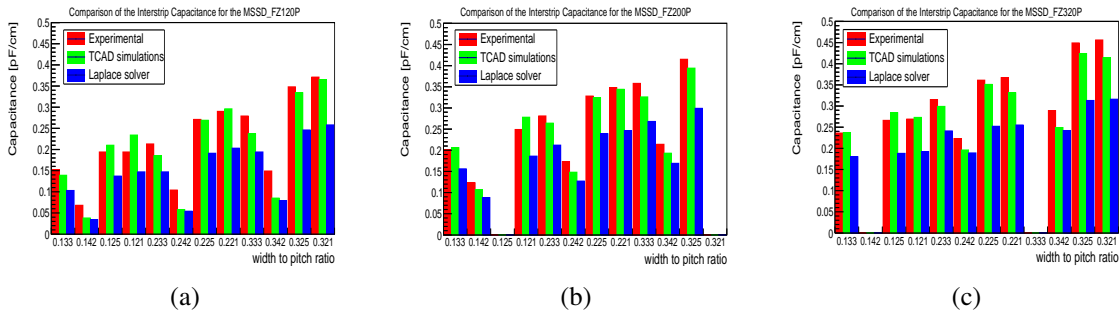


Figure 8: Comparison of the experimental results (red) the results of the related TCAD simulations (green) and the Laplace solver (blue) for the interstrip capacitance in FZ120P 8a, FZ200P 8b and FZ320P 8c sensors.

Figures 9a and 9b show the relative errors of the simulated results (C_{sim}) from our Laplace solver and the TCAD simulations respectively, to the experimental values (C_{exp}) of the interstrip capacitance as it has been calculated with our Laplace solver and with the TCAD simulations,

respectively. The numerical calculations made with the Laplace solver have a mean value of 27% with a standard deviation of 4% while the calculations made with TCAD have mean value of 4% and a standard deviation of 8%.

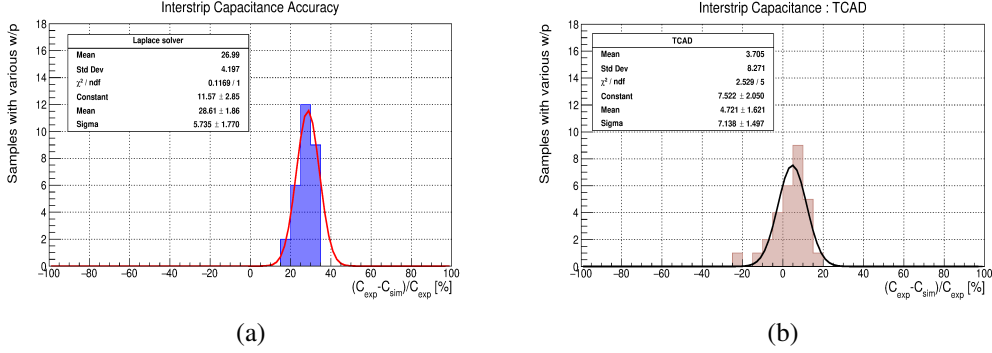


Figure 9: Histograms of the relative error of the simulated results to the experimental values for the interstrip capacitance for the Laplace solver (figure 9a) and for the TCAD simulations (figure 9b).

It must be noted that the numerical calculations from the Laplace solver are tailored to the ideal case where the sensor is free from static charges. In addition, no oxide and no aluminum contacts above the strip plane are taken into account. Thus, it calculates only the capacitance between adjacent implants $C_{I_i-I_j}$. On the other hand, TCAD makes a more detailed simulation with more accurate physical models. Moreover, the interstrip capacitances are calculated by following equation 3.1 where the capacitances between adjacent aluminum $C_{M_i-M_j}$ and between adjacent aluminum and implants $C_{M_i-I_j}$, $C_{I_i-M_j}$ are taken into account. In ref. [10] it is noted that when the metal overhang is absent the implant-implant capacitance is the dominant component of the total interstrip capacitance. Otherwise, when the overhang is present and begins to increase, the other three components of the interstrip capacitance start to increase with a simultaneous decrease of the implant-implant capacitance.

The numerical calculations as described in section 2.2 should calculate the interstrip capacitances in the case where the metal overhang is absent and thus the implant-implant component of the interstrip capacitance is dominant. In order to check the validity of our software in calculating the implant-implant component of the capacitance we have simulated also the case where the metal overhang is absent with TCAD. In this case the aluminum width is taken to be equal to implant width (figure 10). The other properties of the simulated structure were kept the same as described in section 3.1.

Histograms, 11a, 11b, 11c show the simulated results of the implant-implant component of the capacitances for two cases with metal-overhang (depicted in green) and without metal-overhang (depicted in yellow), compared with results from Laplace solver (depicted in blue).

The calculated results of our software agree with the simulated results for the implant-implant components of the interstrip capacitance in the case where metal overhang is absent with an average accuracy of $\approx 7\%$. The implant-implant component of the capacitance decreases in the case where metal overhang is present as it was expected according to [10]. Also changing the values of the

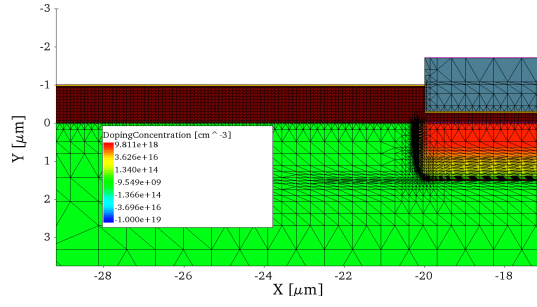


Figure 10: The simulated structure without metal-overhang close to one strip edge. The n-type implant is displayed in red which is simulated with a Gaussian profile, the aluminum contacts are displayed with gray, the SiO_2 is displayed with brown and the p-type silicon bulk is displayed with green.

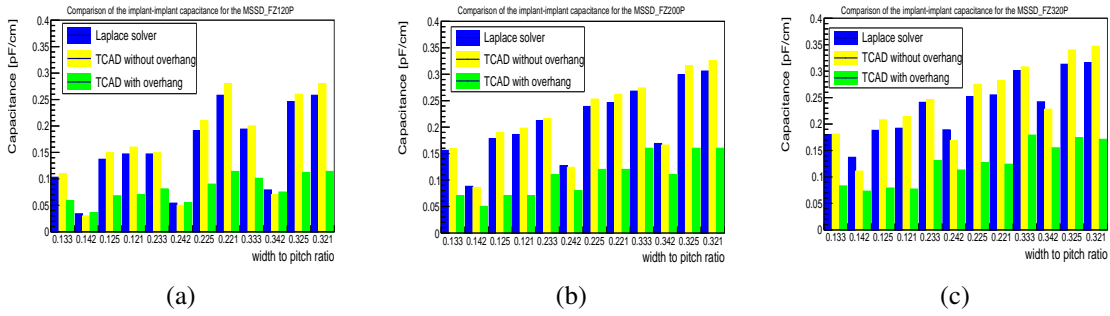


Figure 11: Comparison of the calculated results (blue) with TCAD simulations in the case were metal-overhang is present (green) and without metal-overhang (yellow) for the FZ120P 11a, FZ200P 11b and FZ320P 11c sensors.

dielectric constant of the ambient space to that of SiO_2 doesn't improve the results. However, it slightly decreases the interstrip capacitance while the backplane remains the same.

4.2 Comparison of 3D Laplace solver with experimental data of various pixel geometries

In ref. [13], pixel capacitances have been measured on pixel sensors from 6 different n-type wafers with fixed pitch=100 μm and with varying separation gap between the pixel implants from 5 μm to 30 μm with a 5 μm gap step, resulting in an implant width that ranges from 95 μm to 70 μm . For comparison we have calculated the capacitances for those sensors with our 3D Laplace solver. Figure 12 shows the calculated total interpixel capacitances C_{tip} for the six different structures in comparison with the literature measurements taken from ref. [13]. In this case, due to the square geometry of the pixels and with reference to figure 1, $C_{01} = C_{02}$, while with reference to figure 2 of [13], $C_{01} \equiv C_{ip}$, which is the orthogonal interpixel capacitance and $C_{03} \equiv C_{diag}$ which is the diagonal interpixel capacitance. The data are compared with the total interpixel capacitance, as it is sensed by a virtually grounded preamplifier, given by equation 4.1. The orthogonal (C_{01} , C_{02}) and diagonal C_{03} components are drawn as well for clarity.

$$C_{tip} = 2C_{01} + 2C_{02} + 4C_{03} \quad (4.1)$$

The calculated results approximate the lower error limit of the experimental data of the total interpixel capacitance. The diagonal capacitance in ref. [13] was approximated to 2.7 fF and 3.2 fF on a second fit, which excludes the last experimental data. In our calculations the diagonal capacitance is varied between 1.5 fF for 5 μm gap and 1.0 fF for 30 μm gap. The orthogonal interpixel capacitance in [13] range, between 1 – 2 fF (30 μm gap) to 11 – 12 fF (5 μm gap) while from our calculations the orthogonal capacitance range between 3.37 fF (30 μm gap) to 9.70 fF (5 μm gap).

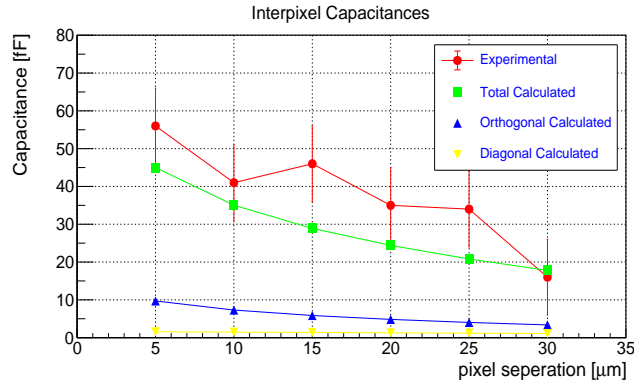


Figure 12: Total interpixel capacitance for sensors with fixed pitch=100 μm and varying separation gap in comparison with experimental data extracted from [13]. Also the calculated results for the orthogonal and the diagonal capacitances are shown.

In ref. [14] pixel capacitances have been measured for irradiated and non-irradiated sensors from LBNL and Atlas/LHC test structures along with simulations with HSPICE [15] and IES Coulomb [16] in two and three dimensions. Each structure includes six 3×9 arrays of rectangular pixels with a 50 μm pitch in their short direction and 536 μm pitch in their long direction. The implant width and the separation gap vary in each test structure. We have calculated the capacitances for the LBNL n-type test structures with the 3D Laplace solver. The experimental and simulated data for the total interpixel capacitance (equation 4.1) reported in [14] in comparison with calculations made with the 3D Laplace solver are presented in figure 13. The Laplace solver results agree with the measurements with a relative error which is less than 32%.

Figure 14 shows the experimental results for the backplane capacitance along with simulation results from IES Coulomb in two and three dimensions and with calculations with our software by using both the two and three dimensional methods. The calculated results from our software are inside the error assessment of ± 5 fF that is noted in ref. [14] expect for arrays 4 and 6 in the 3D case.

The orthogonal interpixel capacitances on the short side are compared with simulated results from IES Coulomb. These results are presented in figure 15a. Also in ref. [14] the second neighbor interpixel capacitances have been calculated. By using the 2D Laplace solver these capacitances were calculated. These results are shown in figure 15b.

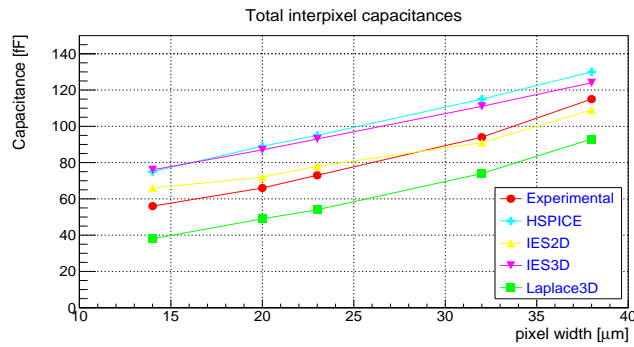


Figure 13: Experimental and simulated data with HSPICE, IES Coulomb in two and three dimensions of LBNL n-type unirradiated sensors extracted from table 2 and table 8 of ref. [14] in comparison with results from Laplace solver in three dimensions for the total interpixel capacitance.

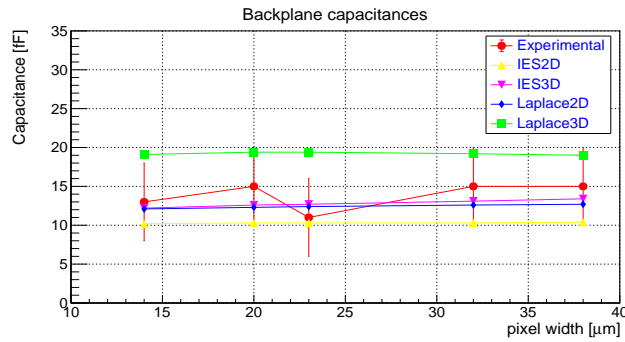


Figure 14: Experimental and simulated data with IES Coulomb in two and three dimensions of LBNL n-type unirradiated sensors extracted from table 6 and of ref. [14] in comparison with results from Laplace solver in two and three dimensions for the backplane capacitance.

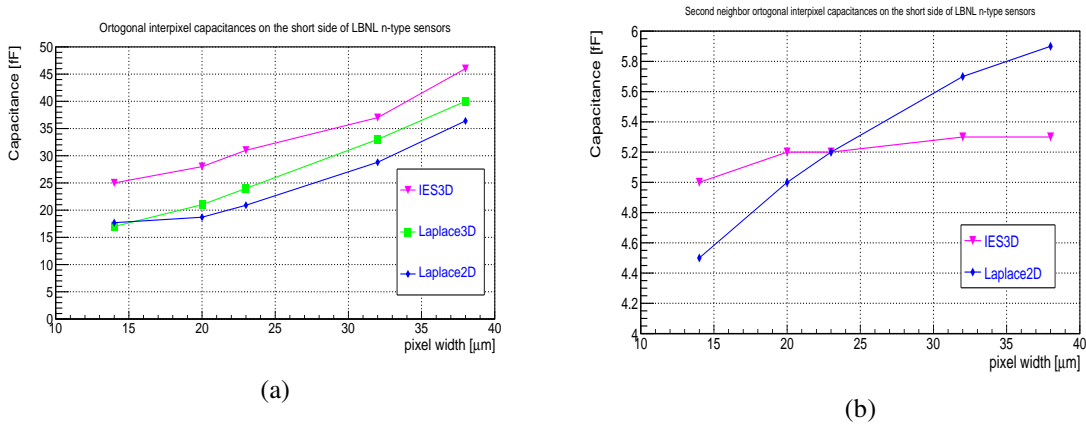


Figure 15: Comparison of simulated data for the orthogonal interpixel capacitance on the short side with results from Laplace solver in three and two dimensions (figure 15a) and comparison of simulated data for the second neighbor capacitance on the short side of LBNL n-type sensors (figure 15b). The simulated data were extracted from table 9 of ref. [14].

4.3 Comparison between TCAD and 3D Laplace solver for various pixel geometries

We have simulated the capacitances for pixel sensors with pixel geometries $50 \times 50 \mu\text{m}^2$ and $100 \times 25 \mu\text{m}^2$ and thicknesses of $150 \mu\text{m}$. These configurations are appropriate to the developmental work in progress for the Phase-2 upgrade of the pixel systems in the CMS/LHC and the ATLAS/LHC experiment at CERN. The separation gaps vary between $5 \mu\text{m}$ to $50 \mu\text{m}$ with a $5 \mu\text{m}$ step size. Simulations were performed by using both TCAD and the 3D Laplace solver. Figure 16 shows the simulated results for the backplane capacitances for sensors with $50 \times 50 \mu\text{m}^2$ pixels and for sensors with $100 \times 25 \mu\text{m}^2$ pixels. The backplane capacitance calculated with the Laplace solver is systematically larger than the one obtained from the TCAD simulations in all the cases for about 1.5 fF . A possible reason for this is the better description of the deep diffusion on the backplane that is simulated with TCAD.

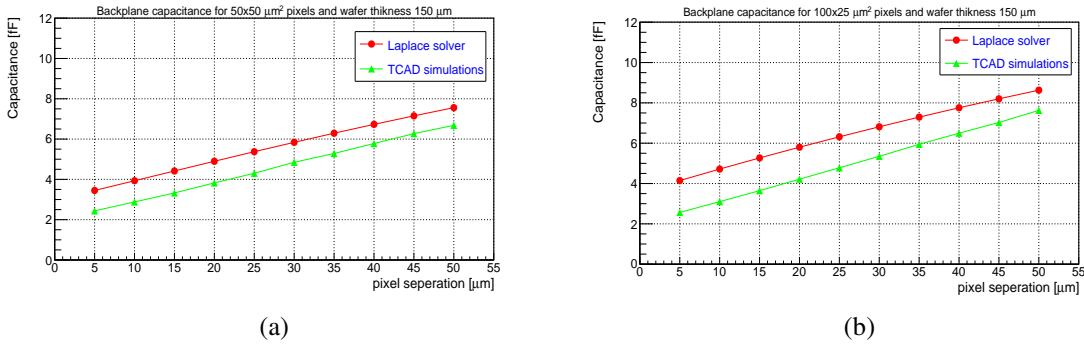
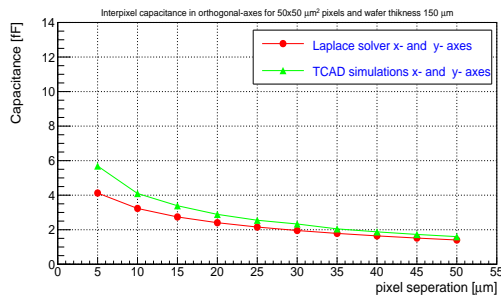


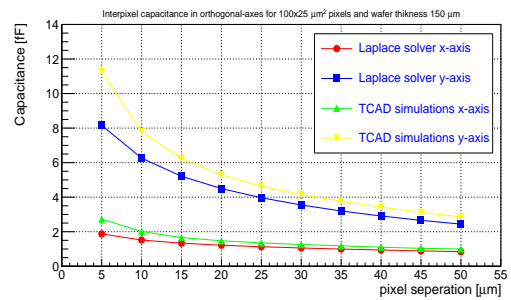
Figure 16: Simulated results by using TCAD (green line) for the backplane capacitance compared with simulated results from our program (red line) which implements the numerical method described in 2.1 for sensors with $50 \times 50 \mu\text{m}^2$ 16a and $100 \times 25 \mu\text{m}^2$ pixel area respectively 16b.

Figures 17 and 18 show the simulated results for the interpixel capacitances. Both simulations show a very good agreement in the calculation of the orthogonal and diagonal interpixel capacitances especially for larger separation gaps. Figure 19 shows the simulated results for the total capacitances, where the total capacitance is the sum of all the total interpixel capacitance (equation 4.1) including the backplane. Again the two simulations agree well in the calculation of the total capacitance especially for gaps larger than $15 \mu\text{m}$.

Figures 20a and 20b show the relative difference between the calculated results with Laplace solver and TCAD simulation results, respectively. It can be noted that the difference between the two simulations decrease with the increase of the separation gap. The relative difference for the backplane capacitance ranges between 29 % and 12 % for sensors with $50 \times 50 \mu\text{m}^2$ pixels and between 38 % and 12 % for sensors with $100 \times 25 \mu\text{m}^2$ pixels. For the orthogonal interpixel capacitances it ranges between 28 % and 12 % for sensors with $50 \times 50 \mu\text{m}^2$ pixels, while for the diagonal capacitances it is less than 2 % and for sensors with $100 \times 25 \mu\text{m}^2$ pixels it ranges between 32 % and 16 % for x- axis and between 28 % and 15 % for y- axis, while for the diagonal capacitances it is less than 3 %. For total capacitance it ranges between 19 % and 0.5 % for sensors with $50 \times 50 \mu\text{m}^2$ pixels and between 19 % and 0.9 % for sensors with $100 \times 25 \mu\text{m}^2$ pixels.

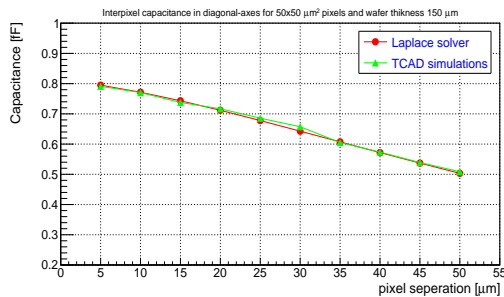


(a)

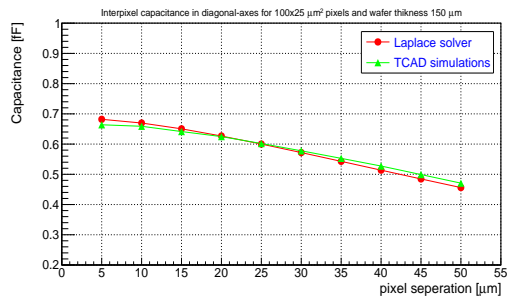


(b)

Figure 17: Simulated results by using TCAD (green-yellow lines) for the orthogonal interpixel capacitance in x- and y- axes, compared with simulated results from our program (red-blue lines) for sensors with $50 \times 50 \mu\text{m}^2$ 17a and $100 \times 25 \mu\text{m}^2$ pixel area respectively 17b .

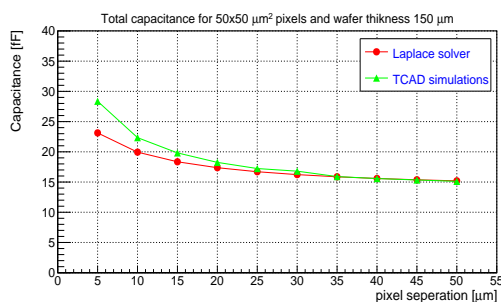


(a)

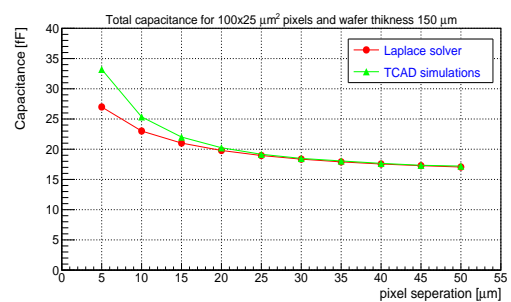


(b)

Figure 18: Simulated results by using TCAD (green line) for the diagonal interpixel capacitance, compared with simulated results from our program (red line) for sensors compared with simulated results from our program (red-blue lines) for sensors with $50 \times 50 \mu\text{m}^2$ 18a and $100 \times 25 \mu\text{m}^2$ pixel area respectively 18b .



(a)



(b)

Figure 19: Simulated results by using TCAD (green line) for the total capacitance, compared with simulated results from our program (red line) for sensors compared with simulated results from our program (red-blue lines) for sensors with $50 \times 50 \mu\text{m}^2$ 19a and $100 \times 25 \mu\text{m}^2$ pixel area respectively 19b.

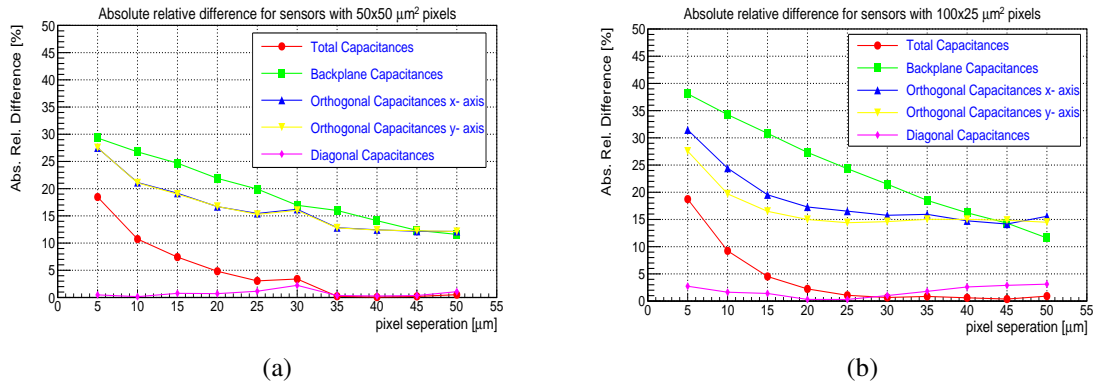


Figure 20: Absolute relative difference between the calculated results with Laplace solver and the TCAD simulation results for sensors with $50 \times 50 \mu\text{m}^2$ 20a and $100 \times 25 \mu\text{m}^2$ pixel area respectively 20b.

4.4 Comparison of the runtime between the two simulations

Table 2 shows the time that is needed to calculate the capacitances by using the Laplace solver. The variable resolution is the number of elements that are used for the numerical calculations. Two examples are given for comparison with TCAD running on an 8-core processor at 3.70 GHz . In the case of strip sensors, for a 2D Laplace resolution of $3.5 \cdot 10^5$, the run time is 7.3 s, while for the TCAD simulation with the same resolution the runtime is 30 min. In the pixel case, for a 3D Laplace resolution of $2.0 \cdot 10^6$ the run time is 34.9 s, while for the TCAD simulations with the same resolution the runtime is 4 h.

Table 2: Calculation time for different values of discretization for pixel and strip sensors.

	resolution	time s
pixel	$2.6 \cdot 10^5$	4.9
	$1.1 \cdot 10^6$	19.2
	$2.0 \cdot 10^6$	34.9
	$4.2 \cdot 10^6$	74.1
strip	$1.0 \cdot 10^3$	0.2
	$1.6 \cdot 10^4$	1.7
	$6.6 \cdot 10^4$	5.3
	$3.5 \cdot 10^5$	7.3
	$5.2 \cdot 10^5$	14.2

5 Conclusion

The fast numerical solution of the Laplace's equation described in this work, gives an accurate approximation of the experimental results and of the TCAD simulations. For the strip sensors the mean value of the relative error of all the regions for the 3 MSSD sensors is 14% for the

backplane capacitance and 27% for the interstrip capacitance, while the implant-implant component for sensors without overhang is approximated with a mean relative error of 7% , compared with TCAD simulation results. For pixel sensors the relative error of the calculations was found to be less than 32% compared to experimental results found in literature. In addition, compared to the TCAD simulations the calculated results show a very good agreement, especially the calculations of the interpixel and total capacitances for large inter-pixel gaps.

As a general conclusion, the program that implements the three and two dimensional numerical solution of the Laplace's equation that is described in this paper can be used in order to provide a fast approximation of detector capacitances for planar silicon strip and pixel sensors before a more detailed simulation with EDA tools is performed. This tool is foreseen to be implemented into a web-based application.

A Properties used for the TCAD simulations

Table 3: Geometrical properties and doping concentrations used for the TCAD simulation of strip sensors.

Material	FZ 120P	FZ 200P	FZ 320P
Bulk doping concentration [cm^{-3}]		$3.5e^{12}$	
Strip doping concentration [cm^{-3}]		$1.0e^{19}$	
Backplane doping concentration [cm^{-3}]		$1.0e^{19}$	
p-stop doping concentration [cm^{-3}]		$1.0e^{16}$	
SiO_2 thickness between strips [μm]		0.95	
SiO_2 thickness between metal-strip [μm]		0.25	
SiN_4 thickness [μm]		0.05	
Aluminum thickness [μm]		0.7	
Strip implant thickness [μm]		1.5	
Error profile backplane depth [μm]	215	125	33

Table 4: Geometrical properties and doping concentrations used for the TCAD simulation of pixel sensors.

Material	n ⁺ p
Bulk doping concentration [cm^{-3}]	$4.0e^{12}$
Pixel doping concentration [cm^{-3}]	$2.0e^{19}$
Backplane doping concentration [cm^{-3}]	$2.0e^{19}$
Guard ring doping concentration [cm^{-3}]	$2.0e^{16}$
SiO_2 thickness [μm]	1.0
Aluminum thickness [μm]	0.7
Pixel implant thickness [μm]	1.5
Error profile backplane depth [μm]	20

Acknowledgments

The authors of this paper would like to thank the outer tracker sensor working group of CMS/LHC for providing the MSSD sensors.

This research is co-financed by Greece and the European Union (European Social Fund- ESF) through the Operational Programme Human Resources Development, Education and Lifelong Learning 2014 2020 in the context of the project "New generation of sensors and electronics for the upgrade of the CMS/LHC experiment at CERN"- MIS 5047807



Operational Programme
Human Resources Development,
Education and Lifelong Learning
Co-financed by Greece and the European Union



References

- [1] S. Kavadias, K. Misiakos and D. Loukas, *Calculation of pixel detector capacitances through three dimensional numerical solution of the Laplace equation*, *IEEE Transactions on Nuclear Science* **41** (1994) 397.
- [2] CMS COLLABORATION collaboration, *The Phase-2 Upgrade of the CMS Tracker*, Tech. Rep. CERN-LHCC-2017-009. CMS-TDR-014, CERN, Geneva, Jun, 2017.
- [3] <https://www.synopsys.com/silicon/tcad.html>, 2019.
- [4] B. Delaunay, *Sur la sphere vide*, *Bulletin de l'Académie des Sciences de l'URSS, Classe des Sciences Mathématiques et Naturelles* **6** (1934) 793.
- [5] Synopsys, *Sentaurus Device User Guide*. Synopsys, Inc.
- [6] S. Sze and G. Gibbons, *Effect of junction curvature on breakdown voltage in semiconductors*, *Solid-State Electronics* **9** (1966) 831 .
- [7] D. Passeri, P. Ciampolini, A. Scorzoni and G. M. Bilei, *Physical modeling of silicon microstrip detectors: influence of the electrode geometry on critical electric fields*, *IEEE Transactions on Nuclear Science* **47** (2000) 1468.
- [8] T. V. Eichhorn, *Development of Silicon Detectors for the High Luminosity LHC*, Ph.D. thesis, U. Hamburg, Dept. Phys., Hamburg, 2015. 10.3204/DESY-THESIS-2015-024.
- [9] R. Eber, *Untersuchung neuartiger Sensorkonzepte und Entwicklung eines effektiven Modells der Strahlenschädigung für die Simulation hochbestrahlter Silizium-Teilchendetektoren*, Ph.D. thesis, 2013. 10.5445/IR/1000038403.
- [10] S. Chatterji, A. Bhardwaj, K. Ranjan, Namrata, A. K. Srivastava and R. Shivpuri, *Analysis of interstrip capacitance of si microstrip detector using simulation approach*, *Solid-State Electronics* **47** (2003) 1491 .
- [11] ATLAS COLLABORATION collaboration, *Technical Design Report for the ATLAS Inner Tracker Pixel Detector*, Tech. Rep. CERN-LHCC-2017-021. ATLAS-TDR-030, CERN, Geneva, Sep, 2017.
- [12] K.-H. Hoffmann, *Campaign to identify the future cms tracker baseline*, *Nuclear Instruments and Methods in Physics Research Section A: Accelerators, Spectrometers, Detectors and Associated E*

- [13] V. Bonvicini, M. Pindo and N. Redaelli, *Junction and interdiode capacitance of silicon pixel arrays*, *Nuclear Instruments and Methods in Physics Research A* **365** (1995) 88.
- [14] G. Gorfine, M. Hoferkamp, G. Santistevan and S. Seidel, *Capacitance of silicon pixels*, *Nuclear Instruments and Methods in Physics Research Section A: Accelerators, Spectrometers, Detectors and Associated E*
- [15] <https://www.synopsys.com/verification/ams-verification/hspice.html>, 20019.
- [16] <https://www.integratedsoft.com/Products/coulomb.aspx>, 20019.